JOURNAL OF AIRCRAFT
Vol. 37, No. 2, March–April 2000

Effect of External Components on V-22 Aircraft Forward-Flight Aerodynamics

Tsze C. Tai*
U.S. Naval Surface Warfare Center, West Bethesda, Maryland 20817

The effects of protuberances, forward-looking infrared, AAR47 sensor fairing, and refueling boom on V-22 forward flight aerodynamics using computational fluid dynamics are investigated. The multizone Navier–Stokes method is applied to the flow over a complete V-22 wing–fuselage–nacelle configuration, with and without external components. The angle of attack varies from 0 to 16 deg in forward flight. A slight increase in drag is found at 0-deg angle of attack for an aircraft configured with the external units; this effect decreases as the angle of attack increases from zero to moderate values. However, at high angles of attack, the added flow disturbances due to attachments seems to worsen tail buffeting and lift-to-drag ratio. The numerical results are in general agreement with recent flight test data.

Introduction

THE aerodynamics of the V-22 aircraft were primarily determined through experiments during the early stages of development.[1–3] Because of its vertical takeoff requirement, the aircraft was designed from the inside out and, thus, had design restrictions that adversely affect its aerodynamic performance. A comprehensive review on the V-22 Osprey aerodynamic development during the past 15 years is given by McVeigh et al.[4] Recently, the use of computational fluid dynamics (CFD) has been explored by the present author to analyze the complex aerodynamics of the V-22 aircraft. The overall flowfield about the aircraft in either hover[5] or forward-flight mode[6–8] has been simulated and analyzed using a multizone, thin-layer, Navier–Stokes solution. The aircraft aerodynamics in hover-to-transition flight mode was explored by Meakin.[9]

Attention is directed toward the forward-flight mode in the present work. Previous analyses[6–8] were based on a clean aircraft configuration. In reality, however, there are various external geometric components or fairings of electronic devices mounted on the fuselage and wing surfaces, as well as some isolated units for the purpose of military operation. These protuberances directly affect the aerodynamic performance and control of the aircraft. The application of CFD serves as an effective means to evaluate these effects, whereas on the other hand, the use of wind-tunnel tests or free-flight tests might be inconvenient and costly.

In the present paper, the aerodynamic effects of an external forward-looking infrared (FLIR) sensor, an AAR47 sensor fairing, and the refueling boom on the V-22 aircraft in forward flight are evaluated. The work is an extension of existing V-22 CFD modeling developed by the present author during the past five years.[6–8] As in the previous work, the steady-state Navier–Stokes solution is carried out in a structured grid with the external geometric components incorporated. Unlike the overset Chimera scheme,[10] the incorporation of the external geometries is performed seamlessly so that grid overlapping and solution interpolation, the two main disadvantages of the Chimera scheme, are avoided completely. The current V-22 aircraft configuration during the engineering manufacturing development phase also include two vortex-generating strakes placed on the forebody ahead of the wing and two wing fences just inboard of the nacelles.[4] The effects of strakes and wing fences are not considered in the present work.

Received 11 February 1999; revision received 20 August 1999; accepted for publication 21 August 1999.

*Senior Research Scientist, Marine and Aviation Department, Carderock Division. Associate Fellow AIAA.

Simulation Method

The simulation method has been described in an early paper.[6] A brief overview of the method is given here.

Grid Generation

A structured, curvilinear, body-conforming grid is employed. The surface grid is constructed from the manufacturer's blueprint with refinement based on data provided by Boeing Defense and Space Group. Figure 1 shows the surface grid for the clean configuration. Although shown in Fig. 1, the tail sections are excluded for simplification in the present work A cylindrical grid topology, which is basically made up of an H–O mixed type with H type in the longitudinal plane and O type in the crossflow plane, is adopted. By assuming zero sideslip, the aircraft is symmetrical about the centerplane and, therefore, only the right half of the aircraft needs to be modeled. (This assumption is valid only in cases of the clean aircraft configuration and the configuration with FLIR and AAR47.) The same multizone, basic grid system developed earlier[6] is retained in the present work. The basic volume grid for the clean configuration, with the outer cylindrical surface set at 8.9 chord lengths from the aircraft centerline, has a total of $179 \times 105 \times 57$ points covering the longitudinal, transverse, and radial directions, respectively.

The NASA Ames 3DGRAPE code[11] is used for basic grid generation, and the CNS/ZONER code[12] is used for zoning and clustering. The latter code has been modified to cluster the viscous region with a variety of spline curves composed of different spacings and numbers for the radial direction to be fitted.

Flow Solver and Turbulence Model

The NASA Langley Research Center thin-layer Navier–Stokes code, namely, the CFL3D code[13] with multizone capability, is used as the basic flow solver. Appropriate modifications to the code for applying specific boundary conditions are implemented. The code is based on a finite volume algorithm with a spatially factored, diagonalized, implicit scheme. The upwind-biased-differencing technique is used for the inviscid terms and central differencing for all viscous terms. The method is globally second-order accurate and well suited for patched grids in a multizone domain.

The code is equipped with a variety of turbulence models including the basic Baldwin–Lomax (B–L) algebraic model,[14] the Spalart–Allmaras one-equation model,[15] and others. The B–L model is used widely throughout the CFD community. Although simple, it is known to be the best model for flowfield dominated by vortical flows. The model was further upgraded with the Degani–Schiff modification.[16] To accommodate the large three-dimensional effects due to complexity of geometry, high angle of attack involved the B–L model has been extended to three-dimensional flows.[8]

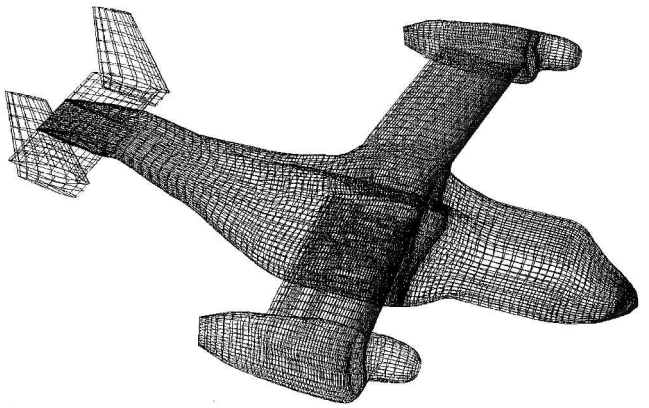

Fig. 1 Surface grid for the V-22 aircraft.

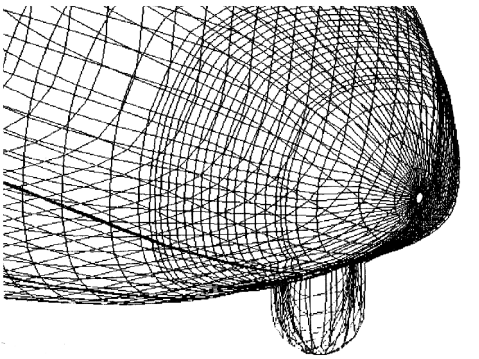

Fig. 2 Surface grid of V-22 aircraft nose with FLIR unit.

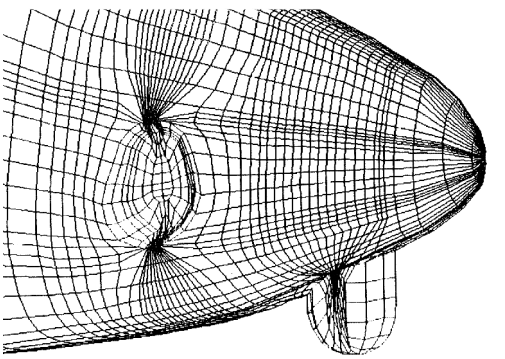

Fig. 3 Surface grid of the V-22 aircraft nose with FLIR and AAR47 components.

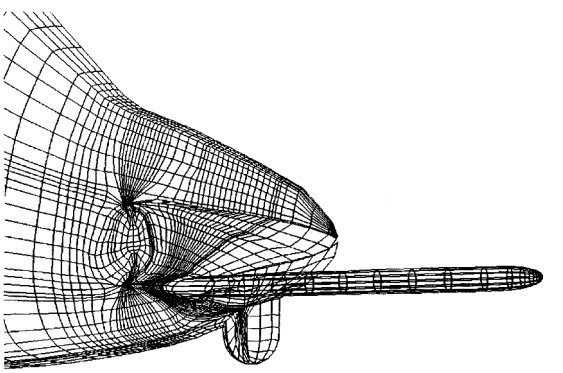

Fig. 4 Surface grid of the V-22 aircraft nose with FLIR, AAR47, and refueling boom.

Multizone Technique and Boundary Conditions

The single basic grid described earlier is eventually divided into multizones for flow solving using the multizone technique. In the literature, the terms multizone and multiblock are generally interchangeable because a particular block of the grid generated is used also as a zone in the flow solving. In the present paper, however, we will distinguish the multizone from multiblock because they are not the same. In the case of the wing–fuselage–nacelle configuration, we have divided the single basic grid into 21 zones for flow solving, whereas the grid was generated with 25 blocks.

The division of the overall mesh into multizones depends primarily on the convenience in applying the boundary conditions. With the same number of radial mesh points for both viscous and inviscid zones, such a division offers exact coincident boundaries between the zones. The main advantage of the approach is that the conservation of the spatial flux of mass, momentum, and energy between the zones is automatically satisfied. A total of 44 interface boundaries are set among the 21 zones for flow solving.

The boundary conditions for the Navier–Stokes flow solver are, within a particular zone, 1) freestream condition imposed at upstream (for the most forward zones only), 2) freestream pressure recovery in downstream (for the most rearward zones only), 3) characteristic form of the inflow–outflow condition at the cylindrical outer boundary, and 4) viscous nonslip flow at all solid surfaces (wing, fuselage, and nacelle). The inlet and outlet of the nacelle are closed for simplicity, and the disk loading and flow swirling at the rotor are neglected. The reason for neglecting the disk loading is that there are only 5–6 ft/s velocity differentials at the rotor disk that may have little effect on the resulting flowfield.

External Components

The external components to be considered here include the FLIR, the fairing of the electronic sensor (AAR47), and the refueling boom. They are described along with the resulting grid changes due to these protuberances.

FLIR

The FLIR unit is a short, hemispherical cylinder mounted upside down directly beneath the aircraft nose. The cylinder has a diameter of about 10.5 in. and a mean height of 12.5 in. Figure 2 shows the surface grid of the nose portion of the aircraft incorporated with the FLIR unit. Grid resolution in the local area has been enhanced in both longitudinal and circumferential directions to accommodate for the increased complexity caused by addition of the unit.

The resulting volume grid has a total of $185 \times 110 \times 57$ points covering the longitudinal, circumferential, and radial directions, respectively. Because the unit is mounted so that its centerline coincides with the aircraft centerplane, the symmetry assumption remains valid and, therefore, only the right half of the aircraft needs to be modeled.

AAR47 Sensor

The fairing of the AAR47 sensor is a raised convex surface geometry with a height of approximately 3.0 in. Shaped like the back of a turtle, the unit is mounted on the side of the aircraft nose below the front of the windshield panel, one on each side. Thus, the assumption of symmetry still holds. The size of the volume grid is increased to $203 \times 115 \times 57$ when the AAR47 fairing is implemented. Figure 3 shows the detail of the nose surface grid with the FLIR and AAR47 components incorporated. (The geometry of the AAR47 sensor fairing has been modified by Boeing after the present work. The new shape has an elongated rear portion that will be incorporated in the CFD model in the near future.) The components are embedded seamlessly in the main surface with no increase in complexity in flow solving.

Refueling Boom

Unlike the FLIR and AAR47 units, the refueling boom is installed on the right side of the nose only. It is a 69-in.-long blunted ogive-cylindrical tube having a diameter of 4.5 in. The boom is mounted between the FLIR and AAR47 units (see Fig. 4). Because of the

one-sided location of the boom, the assumption of symmetry is no longer valid and, therefore, the whole aircraft must be modeled. The size of the volume grid is increased to 215 × 231 × 57, which is more than double the size of the earlier grid. Because of increased complexity, the nose portion of the overall grid is completely revised to incorporate the boom. Again, the gridding is accomplished in a seamless manner. The number of zones for the flow solving is increased from 21 to 45.

Results and Discussion

The steady-state results are obtained for the following four cases: 1) the clean configuration, 2) the configuration with the FLIR added, 3) the configuration with both the FLIR and AAR47 fairing added, and 4) the configuration with the FLIR, AAR47, and the refueling boom added. For the first three cases, the freestream Mach number is set at 0.209 with the angle of attack varying at 0, 7, and 16 deg. These conditions yield a Reynolds number of 12.4×10^6 based on the wing chord length of 8.33 ft, or 1.87×10^6 for a 15% scale model. The Mach 0.209 freestream speed was chosen to match the flow conditions used in wind-tunnel tests of a 15% scale model at Boeing, although the free-flight tests' Mach numbers are generally much higher. For case 4, the freestream Mach number is set at Mach 0.345 to match the flight test condition at a freestream of 228 kn. In all of these cases, the flow Reynolds numbers fall well within the fully turbulent flow range, and so a fully turbulent flow was assumed.

A converged steady-state solution requires 4500–5500 iterations (time steps) that amount to approximately 10–12 h of Cray C-90 CPU time for the half-aircraft model. The CPU time becomes doubled for the whole aircraft model with the refueling boom embedded. All computations were performed on the Department of Defense high-performance computing facilities at the Naval Oceanographic Center and the Air Force Aeronautical Systems Center. Convergence is reached when both lift and drag coefficients asymptotically approach constant values. This is usually the case when the Spalart–Allmaras turbulence model is used. For most cases that were computed based on the modified B–L model, the results were considered to be converged when the lift and drag coefficients fluctuated only within a narrow band. The fluctuation is believed to be caused by shifting of vortex cores created by massive crossflow (vortex-layer-type) separation.

Effect of FLIR

For the case of Mach 0.209 at zero angle of attack, the overall pressure distributions for both the clean configuration and the configuration with FLIR are almost identical except in the local area where the FLIR is embedded. The FLIR's face has high pressures, whereas its rear side is subject to low pressures (see Fig. 5). This results in an increase in drag coefficient of about 1.5% compared to the clean configuration. (The relative value of the force coefficients is used to avoid any confusion in choosing the proper reference area used in calculation of these coefficients.) This amount of drag increase, which could be solely due to the added FLIR geometry itself, agrees well with the manufacturer's estimate. The difference in lift

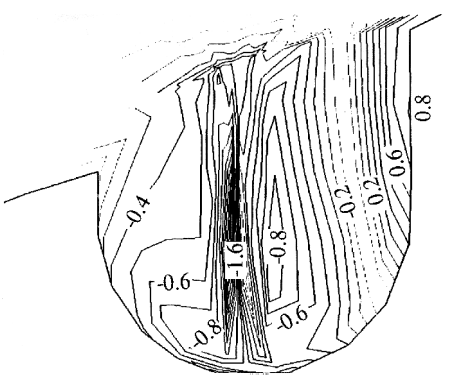

Fig. 5 Pressure coefficients on the FLIR unit.

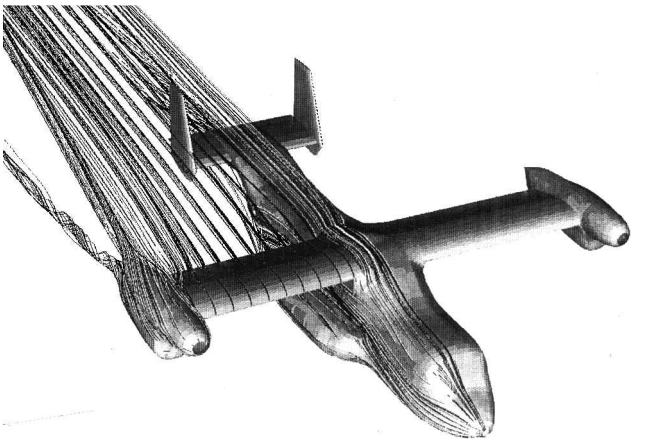

Fig. 6 Particle traces over the clean V-22 configuration at $M_\infty = 0.209$ and $\alpha = 7$ deg.

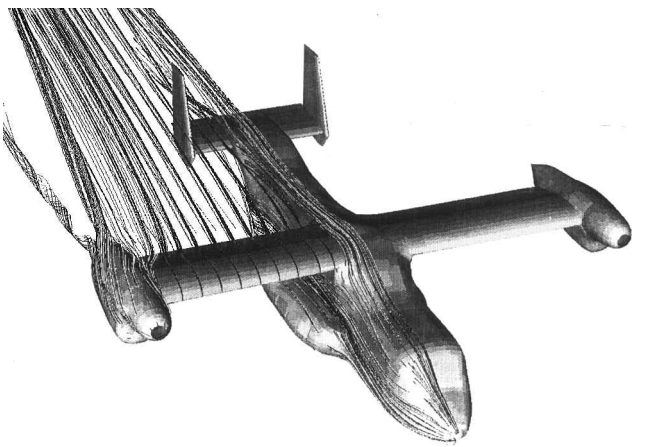

Fig. 7 Particle traces over V-22 configuration with FLIR at $M_\infty = 0.209$ and $\alpha = 7$ deg.

coefficients for the two configurations is insignificant at 0-deg angle of attack.

The effect of FLIR becomes more visible with the aid of the resulting flow patterns. These flow patterns are depicted by particle traces of the instantaneous streamlines emanating from various stations at the fuselage, wing, and nacelle. At an angle of attack of 7 deg (cruise flight), the particle traces reveal that the flow patterns are similar in both configurations, except that streamlines over the upper rear fuselage of the configuration with FLIR tend to be closer to the surface (see Figs. 6 and 7). The phenomenon could be caused by vortices generated due to the presence of FLIR, which, incidentally, serves as a vortex control device. Indeed, the FLIR enhances the lift a small amount (about 0.5%) as one compares the lift coefficients of the two configurations traveling at this particular speed and angle of attack. The effect of vortices, however, is too small to offset the added drag due to the FLIR, and so the lift-to-drag ratio is about the same as that of the clean configuration.

This favorable effect (increased lift) quickly disappears as the angle of attack increases. At an angle of attack of 16 deg (maneuvering flight), flow separation over the upper wing surface becomes massive and large crossflows flowing inboard are apparent. The crossflow mixes with the main stream over the fuselage, which in turn contributes to the swirling of the flow as it proceeds downstream [see Fig. 8 (clean configuration)].

The flow separation appears to be worsened by the presence of the FLIR geometry as evidenced by extensive flow swirling over the overwing fairing compared with that of the clean configuration (see Fig. 9). The lift coefficient of the configuration with the FLIR becomes, as a consequence, slight lower than that without the FLIR. Because flow separation over the wing has a direct impact on tail

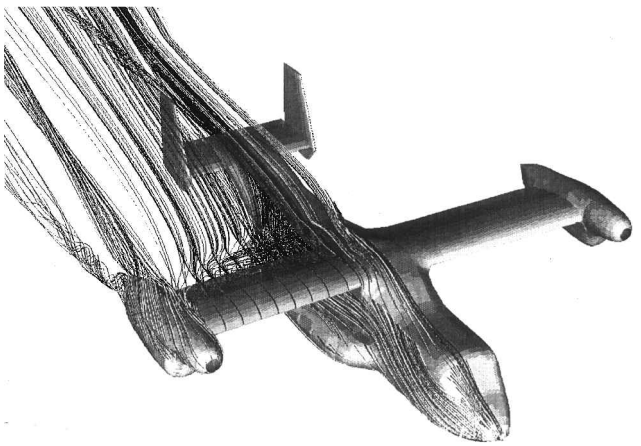

Fig. 8 Particle traces over the clean V-22 configuration at $M_\infty = 0.209$ and $\alpha = 16$ deg.

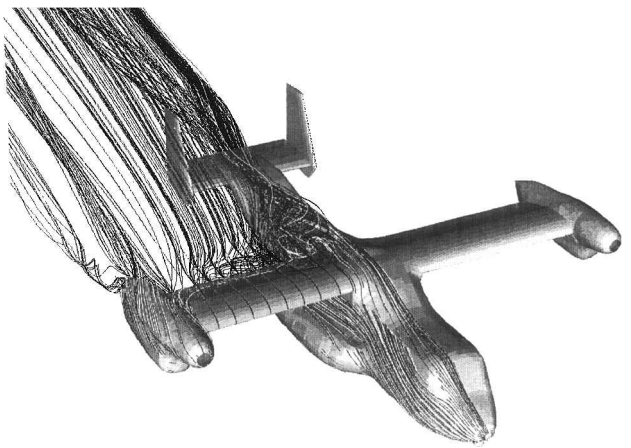

Fig. 9 Particle traces over V-22 configuration with FLIR unit on at $M_\infty = 0.209$ and $\alpha = 16$ deg.

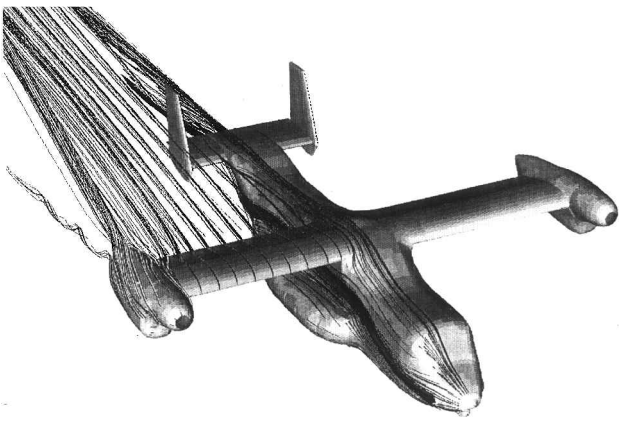

Fig. 10 Particle traces over V-22 configuration with FLIR and AAR47 units at $M_\infty = 0.209$ and $\alpha = 7$ deg.

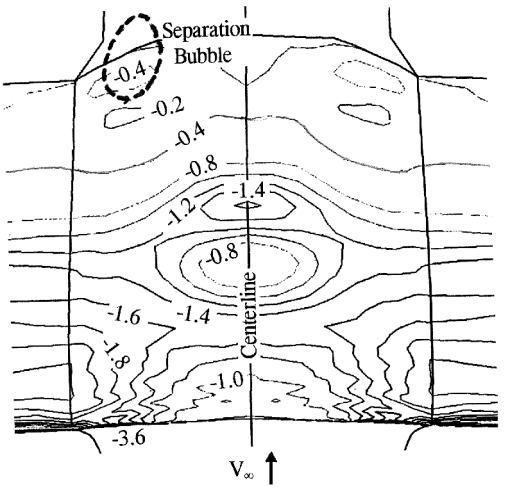

Fig. 11 Pressure distribution over the overwing fairing (configuration with FLIR and AAR47, $\alpha = 7$ deg).

buffeting,[6,7] the FLIR seems to have an adverse effect on tail buffeting at high angle of attack. That is, the onset of a tail buffet may occur at an angle of attack 1 or 2 deg earlier with the FLIR installed.

Effect of FLIR and AAR47

As opposed to the FLIR ball, the addition of the AAR47 fairing has very little effect on the drag at zero angle of attack. This is because the unit is relatively thin compared with the FLIR and appears to be more streamlined. The added drag may be compensated by the favorable effect due to the free vortices created. The net lift-to-drag ratio is unchanged at zero angle of attack.

At a moderate angle of attack of 7 deg, more vortices are generated that enhance the favorable effect on lift and drag. The particle traces of the flow over the configuration with both FLIR and AAR47 on (see Fig. 10) reveal that the flow pattern resembles that of the configuration with FLIR alone (Fig. 7). The streamlines over the fuselage remain close to the surface. As in the earlier case, this is beneficial for lift: An increase of 0.5% in lift is obtained as compared with the clean configuration. Furthermore, the streamlines from AAR47 pass through the middle portion of the lower fuselage–sponson area where some flow separation may have been suppressed or eliminated by the vortices due to AAR47. A small change in drag coefficient is noted as compared with the clean configuration. The lift-to-drag value changes from 7.65 for the clean configuration to 7.61 with the FLIR and AAR47 units. (Here we are using numerical values because the ratio is independent of the reference area.) These values are within the range seen in flight tests data (S. A. Woods, M. A. McVeigh, C. Keys, and J. Liu, Naval Air Systems Commands, Patuxent River, MD, and The Boeing Company, Philadelphia, PA, August–September 1998, private communications). This small change in magnitude implies that there are almost no penalties in adding these external components in cruise flight.

The corresponding pressure distribution over the overwing fairing is shown in Fig. 11. The overwing fairing is a good area to examine the flow separation because of its geometric location, as well as its highly bumpy contour in the vicinity of the centerline. The pressure peak at the leading edge of the fairing yields a pressure coefficient value of -3.6 (i.e., the local velocity has accelerated to approximately 1.6 times the freestream speed), a peaky velocity desirable for favorable flow development over an airfoil.[17]

Generally, the flow is mostly attached over the fairing, except in the rear corner region where a bubble-type flow separation is detected with the aid of velocity profiles in the region. (The bubble-type separation is due to vanishing skin friction.[6]) The location of the bubble is given in Fig. 11. Inside the viscous shear layer, the flow reverses at the leading edge of the bubble and reattaches at the trailing edge of the bubble. The separation is classified as minor because it is confined locally and does not contain sufficient crossflow to trigger a vortex-type separation. (The vortex-type separation is caused by convergence of streamlines in the spanwise direction.[6]) Although not shown, similar local flow separation takes place in the case of the clean configuration and the configuration with the FLIR ball as well. Addition of AAR47 seems to impose no change in the effect on this local phenomenon. Outside the bubble, the flow is attached.

Figure 12 shows the velocity vectors along the line of symmetry of the fairing, which is also the aircraft centerline. There are no reversed velocity vectors regardless of its bumpy curvature. Away from the centerline, however, the velocity profile contains reversed

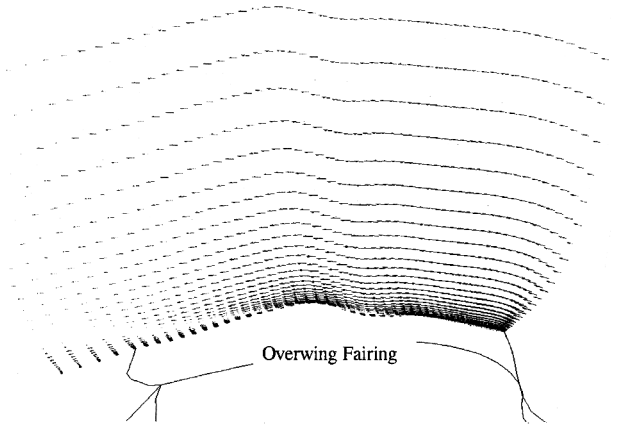

Fig. 12 Velocity vectors along overwing fairing centerline (configuration with FLIR and AAR47, α = 7 deg).

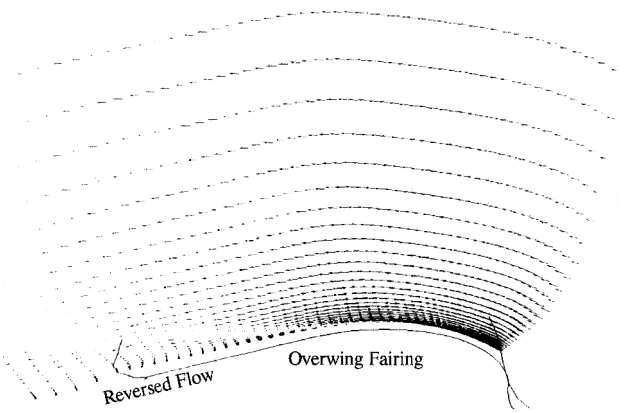

Fig. 13 Velocity vectors along a chord on overwing fairing (configuration with FLIR and AAR47, α = 7 deg).

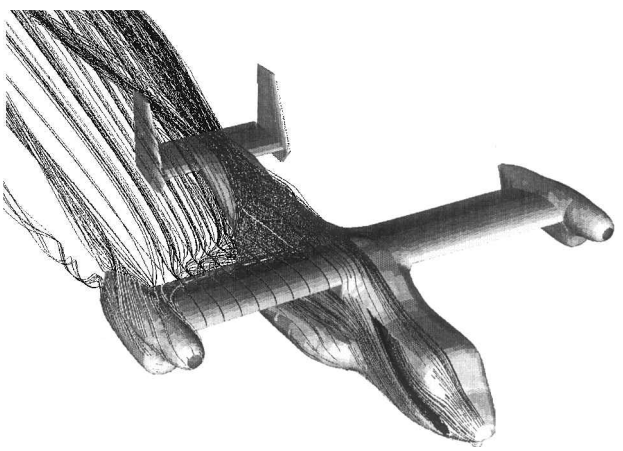

Fig. 14 Particle traces over V-22 configuration with FLIR and AAR47 units at M_∞ = 0.209 and α = 16 deg.

vectors in the rear corner region (see Fig. 13). This is in confirmation with the pressure contours of Fig. 11 that exhibit a local bubble-type separation in the region.

As the angle of attack increases, these benefits gradually disappear because of worsened flow separation. At a 16-deg angle of attack, the streamlines from AAR47 proceed to the upper fuselage, mix with those from forward fuselage, and finally separate from the surface aft of the wing–fuselage juncture (see Fig. 14). The separated flow now contains both the bubble- and vortex-type separations; the latter prevails over the former. The vortex-type separation has been caused by the large crossflow[18] from the wing due to high angle of attack. Characterized as open separation in three dimensions,[19,20] the onset of the vortex-type separation is determined by convergence of

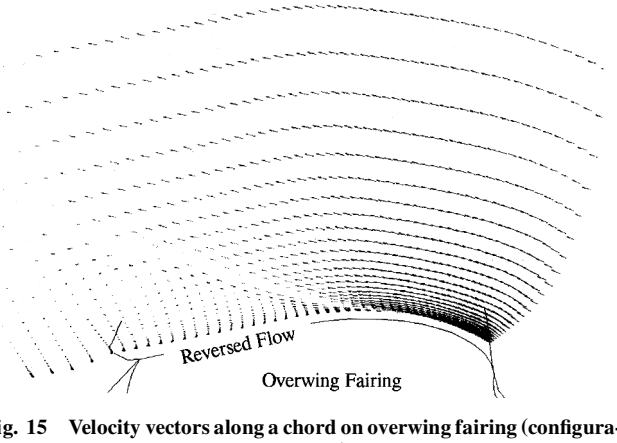

Fig. 15 Velocity vectors along a chord on overwing fairing (configuration with FLIR and AAR47, α = 16 deg).

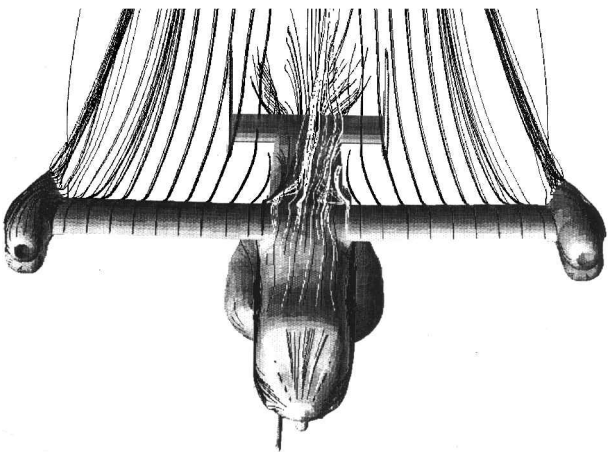

Fig. 16 Particle traces over V-22 configuration with FLIR, AAR47, and refueling boom at M_∞ = 0.345 and α = 7 deg, forward view.

streamlines rather than vanishing skin friction. The size of separated flow region extends to almost half of the overwing fairing as indicated by the extensive flow reversal shown in Fig. 15. The massive flow separation also leads to much worsened tail buffeting. The lift coefficient has decreased to about 1% below the clean configuration level, whereas the drag coefficient remains unchanged. There is a net reduction in the lift-to-drag ratio from 5.11 for the clean configuration value, to 5.03, for the present configuration. Again, these lift-to-drag values are within the range of flight tests data described in the private communications cited earlier.

Effect of Refueling Boom

The effect of the refueling boom is evaluated with the FLIR and AAR47 units on. There are two reasons for doing so: 1) for convenience, because it is a natural extension of the earlier case and 2) for practical purposes because the refueling boom is optional equipment only for a special version of the aircraft whereas the FLIR and AAR47 units are standard. In other words, a V-22 aircraft with a refueling boom must have the FLIR and AAR47 units already installed (not vice versa). In evaluating the effect of the boom, therefore, we have to make comparisons of the results with that of the configuration with the FLIR and AAR47 geometries on.

One obvious effect of the boom is that the flow is no longer symmetric with respect to the aircraft centerplane. Figure 16 shows the particle traces of the flow over this configuration at Mach 0.345 and angle of attack of 7 deg in a forward view. The flow patterns over the configuration are in deviation from total symmetry; streamlines over the fuselage and overwing fairing region tend to proceed toward the left side of the aircraft. There is also a slight reduction in velocity at the leading edge of the overwing fairing that seems to be caused by the boundary-layer development around the boom.

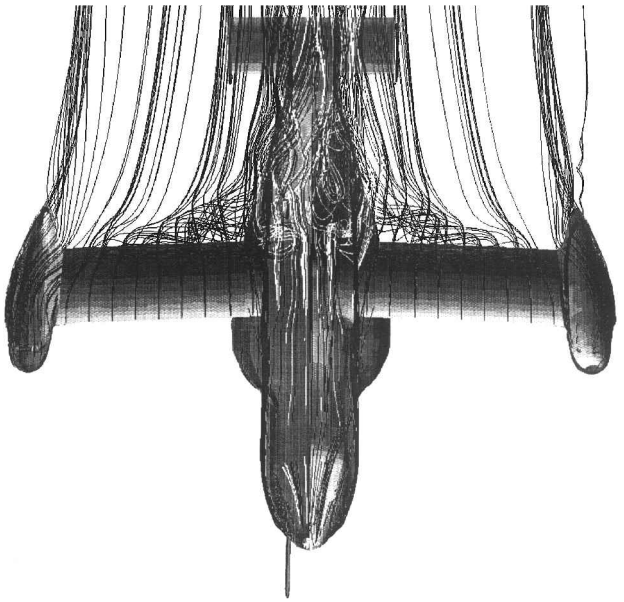

Fig. 17 Particle traces over V-22 configuration with FLIR, AAR47, and refuel boom at M_∞ = 0.345 and α = 16 deg.

The resulting lift coefficient is slightly higher on the right-hand side than that on the left-hand side, even where there is no side slip. Although the direct viscous drag due to the boom itself is insignificant, the total drag is increased by flow separation. It leads to a lower lift-to-drag ratio at this angle of attack by up to 5%, compared to that of the configuration with the FLIR and AAR47 units only. The difference, although largely due to the addition of the boom, may include the effect of gridding changes in the nose portion as mentioned in the section "External Components."

As the angle of attack increases to 16 deg, flow separation worsens in general, but more so on the left-hand side than on the boom side. Figure 17 shows the particle traces over the configuration at Mach 0.345 and angle of attack of 16 deg. The added flow disturbance will likely worsen the onset and severity of tail buffeting. Because of unevenness of the flow, the vertical tail on the left-hand side would experience buffeting more than the right-hand side would. By the same token, as the gap in lift between the two sides of the wing becomes widened, the right wing has a slightly higher lift than the left wing. Again, there is also an up to 5% reduction in lift-to-drag ratio compared to the configuration with FLIR and AAR47 units.

Conclusions

The effect of external protuberances on the V-22 aircraft forward-flight aerodynamics is investigated by using a multizone, thin-layer, Navier–Stokes method. Based on results obtained, which have been qualitatively compared with flight test data, some conclusions may be drawn:

1) The FLIR unit causes a slight increase in drag coefficient at a 0-deg angle of attack. This penalty decreases as the angle of attack increases, possibly due to a favorable vorticity effect. At high angles of attack, however, added flow disturbance introduced by the FLIR will likely worsen tail buffeting and reduce the lift-to-drag ratio.

2) Vortices created by addition of the FLIR and AAR47 units produce a favorable effect on lift at moderate angle of attack, resulting in a small change in lift-to-drag ratio. As the angle of attack increases, the effect becomes unfavorable due to the worsened flow separation that leads to earlier tail buffet onset and reduces the lift-to-drag ratio.

3) When the refueling boom is added, the flow becomes asymmetric because of the one-sided location of the boom. The right wing (boom side) produces slightly higher lift than the left wing. The effect of the refueling boom remains unfavorable in the range of the angle of attack considered.

Acknowledgment

The present work was supported by the Naval Air Systems Command (Airtask A511 5115 010D 3H142 50000) under the cognizance of S. A. Woods. The Department of Defense High Performance Computing facilities located at Naval Oceanographic Center and Air Force Aeronautical Systems Center provided the Cray C-90 CPU time. The author wishes to thank M. A. McVeigh of Boeing Helicopters Division for useful comments, T. L. Wood of Bell Helicopters for providing the FLIR and AAR47 geometries, and D. Grove of the Naval Air Systems Command for providing the coordinates of the refueling boom.

References

[1]Blohm, R., and Bartie, K., "V-22 Aerodynamic Report," Rept. 901-909-632, Bell–Boeing Tiltrotor Team, Philadelphia, PA, July 1986.

[2]McVeigh, M. A., Grauer, W. K., and Paisley, D. J., "Rotor Airframe Interactions on Tiltrotor Aircraft," *Journal of American Helicopter Society*, Vol. 35, No. 3, 1990.

[3]Grauer, W. K., and Farrell, M. K., "V-22 Flight Test Aerodynamics," *Proceeding of the 47th Annual Forum of the American Helicopter Society*, Vol. 1, American Helicopter Society, Washington, DC, 1991, pp. 101–106.

[4]McVeigh, M. A., Liu, J., O'Toole, S. J., and Woods, S. A., "V-22 Osprey Aerodynamic Development—A Progress Review," 22nd European Rotorcraft Forum, Paper 2225, Sept. 1996; also *Aeronautical Journal*, Vol. 101, No. 1006, 1997, pp. 231–244.

[5]Tai, T. C., and Vorwald, J., "Simulation of V-22 Rotorcraft Hover Flowfield," AIAA Paper 93-4878, Dec. 1993.

[6]Tai, T. C., "Simulation and Analysis of V-22 Tiltrotor Aircraft Forward-Flight Flowfield," *Journal of Aircraft*, Vol. 33, No. 2, 1996, pp. 369–376; also AIAA Paper 95-0045, Jan. 1995.

[7]Tai, T. C., "Simulation and Analysis of V-22 Aircraft Maneuvering Aerodynamics," AIAA Paper 96-2477, June 1996.

[8]Tai, T. C., "Extension of Baldwin-Lomax Turbulence Model to Three-Dimensional Flows," AIAA Paper 97-0209, Jan. 1997.

[9]Meakin, R., "Moving Body Overset Grid Methods for Complete Aircraft Tiltrotor Simulations," AIAA Paper 93-3350, July 1993.

[10]Benek, J. A., Steger, J. L., Dougherty, F. C., and Buning, P. G., "Chimera: A Grid-Embedding Technique," AEDC-TR-85-64, Arnold Engineering Development Center, Arnold Air Force Station, TN, April 1986.

[11]Sorenson, R. L., "The 3DGRAPE Book: Theory, Users' Manual, Examples," NASA TM 102224, July 1989.

[12]Flores, J., and Holst, T. L., "Numerical Solution of the Navier–Stokes Equations for Complex Configurations," *Lecture Series in Computational Fluid Dynamics*, Univ. of Tennessee Space Inst., Tulahoma, TN, 1988, pp. 1–97.

[13]Thomas, J. L., Krist, S. T., and Anderson, W. K., "Navier–Stokes Computations of Vortical Flows over Low-Aspect-Ratio Wings," *AIAA Journal*, Vol. 28, No. 2, 1990, pp. 205–212.

[14]Baldwin, B., and Lomax, H., "Thin-Layer Approximation and Algebraic Model for Separated Turbulent Flow," AIAA Paper 78-0257, Jan. 1978.

[15]Spalart, P., and Allmaras, S., "One-Equation Turbulence Model for Aerodynamic Flows," AIAA Paper 92-0439, Jan. 1992.

[16]Degani, D., and Schiff, L. B., "Computation of Supersonic Viscous Flows Around Pointed Bodies at Large Incidence," AIAA Paper 83-0034, Jan. 1983.

[17]Pearcey, H. H., "The Aerodynamic Design of Section Shapes for Swept Wings," *Advances in Aeronautical Sciences*, Vol. 3, Pergamon, New York, 1961, pp. 277–322.

[18]Tai, T. C., "Effect of Crossflow on the Vortex-Layer-Type Three-Dimensional Flow Separation," *Three-Dimensional Turbulent Boundary Layers*, edited by H. Fernholz and E. Krause, Springer–Verlag, New York, 1982, pp. 117–125.

[19]Maskell, E. C., "Flow Separation in Three Dimensions," Rept. Aero 2565, Royal Aircraft Establishment, Bedford, England, U.K., Nov. 1955.

[20]Wang, K. C., "New Developments in Open Separation," *Three-Dimensional Turbulent Boundary Layers*, edited by H. Fernholz and E. Krause, Springer–Verlag, New York, 1982, pp. 94–105.